Oxygen electronic screening and hybridization determining the insulator-metal transition of $Eu_{1-x}Ba_xTiO_3$

Xiao Chi,[1,2] Km Rubi,[1] Anindita Chaudhuri,[2,3] Lai Mun Wong,[4] Xiaojiang Yu,[2] Caozheng Diao,[2] Anil Kumar,[1] Mark B. H. Breese,[1,2] Shijie Wang,[1,4] Ramanathan Mahendiran,[1,*] and Andrivo Rusydi[1,2,3,5,†]

[1]*Department of Physics, 2 Science Drive 3, National University of Singapore, Singapore 117542, Singapore*

[2]*Singapore Synchrotron Light Source, National University of Singapore, 5 Research Link, Singapore 117603, Singapore*

[3]*NUSSNI-NanoCore, National University of Singapore, Singapore 117576, Singapore*

[4]*Institute of Materials Research and Engineering, A*-STAR, 2 Fusionopolis Way, Singapore 138634, Singapore*

[5]*National University of Singapore Graduate School for Integrative Sciences and Engineering (NGS), 28 Medical Drive, Singapore 117456, Singapore*

(Received 24 June 2017; revised manuscript received 16 May 2018; published 30 August 2018)

An insulator-metal transition (IMT) is a fascinating yet hotly debated phenomenon in condensed-matter physics. Here we report on the evolution of electronic structure across IMT as in $Eu_{1-x}Ba_xTiO_3$ as a function of x ($x = 0$ for ETO and $x = 0.5$ for EBTO) and temperature comprehensively using high-resolution spectroscopic ellipsometry, soft x-ray absorption spectroscopy at Ti L and O K edges, and transport measurements. We observe different types of spectral weight transfers (SWTs), which are responsible for tuning optical band gaps, accompanied by dramatic changes in electrical conductivity. At room temperature, when x increases, SWT occurs due to the high energy of O $2p$ to low-energy bands. Such a SWT increases Eu-O-Ti hybridization and enhances Drude response, which increases electrical conductivity in EBTO. Interestingly, upon cooling, SWT arises from low-energy to high-energy bands and opens up a gap of a low-energy oxygen band, which then suppresses electrical conductivity in EBTO. We argue that the unscreened electron-electron interaction in oxygen yields a metal-to-charge-transfer insulator-like transition. Our result reveals comprehensively the importance of oxygen screening effects and hybridizations in the IMT, and it provides insight into $Eu_{1-x}Ba_xTiO_3$.

DOI: 10.1103/PhysRevB.98.085152

I. INTRODUCTION

In condensed-matter physics, an insulator-metal transition (IMT) phenomenon remains one of the hot topics in fundamental science as well as applications. Even though an IMT has been observed in a number of transition-metal oxides, including manganites [1–4], vanadites [5–8], and nickelates [9,10], its origin remains hotly debated.

The perovskite-structure half-doped compound europium barium titanate, $Eu_{0.5}Ba_{0.5}TiO_3$, was predicted to be ferroelectric and ferromagnetic and was suggested to be one of the most promising multiferroics almost 40 years ago [11]. The parent materials are europium titanate ($EuTiO_3$) and barium titanate ($BaTiO_3$). Both Eu and Ba are divalent. $EuTiO_3$ is antiferromagnetic and quantum paraelectric and has seven unpaired and localized electrons in Eu $4f$ orbitals, which might result in a large spin magnetization of $7\mu_B$ per one Eu^{2+}. $BaTiO_3$, on the other hand, is nonmagnetic and an ideal ferroelectric [12]. Thus, with the coupling between magnetism and dielectric properties [13], $Eu_{1-x}Ba_xTiO_3$ may possess a rich diversity of physical properties. Ferroelectric (Eu,Ba)TiO_3 has been proposed for searching an electron electric-dipole moment (EDM) [14]. The electric-dipole-moment phenomenon has indeed been observed in polycrystalline $Eu_{0.5}Ba_{0.5}TiO_3$, in which dielectric and electrical polarization measurements have shown a ferroelectric phase below $T_{FE} = 215$ K and an antiferromagnetic phase below $T_C = 1.9$ K [15]. Moreover, when the $Eu_{0.5}Ba_{0.5}TiO_{3-\delta}$ was doped by electrons via oxygen vacancies, a ferromagnetic ground state could be generated [16].

Here, we report large changes of electrical properties with an IMT-like transition and an evolution of electronic structure and spectral weight transfer (SWT) across IMT in $Eu_{1-x}Ba_xTiO_3$ as a function of Ba ($x = 0$ or ETO and $x = 0.5$ or EBTO) and temperature. Our transport measurement shows changes of electrical conductivity by one to three orders of magnitude as a function of doping and temperature. The SWT, which is a fingerprint of electronic correlation [17–21], and the electronic structure are directly probed using a combination of soft x-ray absorption spectroscopy (XAS) at Ti $L_{2,3}$ and O K edges, high-resolution spectroscopic ellipsometry (SE), and transport measurements [22,23]. From the analysis of different SWT phenomena, we reveal the important role of the hybridizations and the electronic screenings of oxygen in determining IMT in $Eu_{1-x}Ba_xTiO_3$.

II. SAMPLES PREPARATIONS AND EXPERIMENTAL METHODS

Polycrystalline $EuTiO_3$ (ETO) and $Eu_{0.5}Ba_{0.5}TiO_3$ (EBTO) samples were synthesized using a solid-state reaction method with a stoichiometric mixture of Eu_2O_3, $BaCO_3$, and TiO_2

*phyrm@nus.edu.sg

†Author to whom all correspondence should be addressed: phyandri@nus.edu.sg

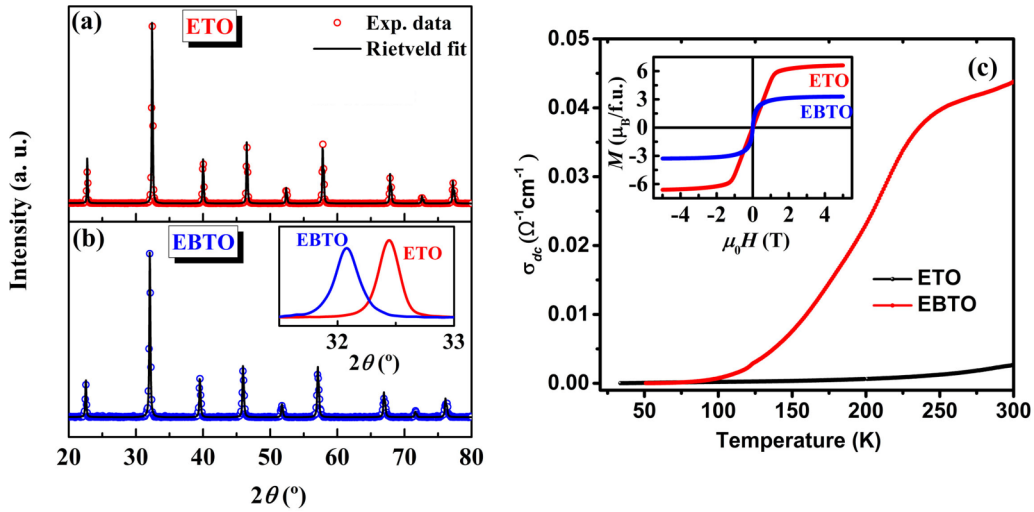

FIG. 1. Room-temperature powder x-ray diffraction pattern for (a) ETO and (b) EBTO. The symbols and lines represent the experimental data and Rietveld fit, respectively. The inset of (b) shows an enlarged view of the comparison of the peak position for both compounds. (c) Temperature dependence of dc conductivity, σ_{dc}, and inset: magnetic-field dependence of magnetization (M) for ETO and EBTO.

in a reduced atmosphere (95% Ar and 5% H_2). The phase and crystal structure of the samples are examined via powder x-ray diffraction (XRD) using Cu $K\alpha$ radiation, and TOPAS software was used for data refinement. Figures 1(a) and 1(b) show powder XRD patterns with a Rietveld fit for ETO and EBTO, respectively. From our analysis, we find that Ba substituted for Eu, consistent with magnetization data [see the inset of Fig. 1(c)]. Both samples crystallize in a cubic structure with a $Pm\bar{3}m$ space group. The lattice constant (a) values of EBTO ($a = 3.9599$ Å) are slightly larger than those of ETO ($a = 3.9056$ Å). The increase in the a value of EBTO is most likely due to the larger ionic radius of Ba^{2+} (1.35 Å) than that of Eu^{2+} (1.17 Å). Four-probe dc resistivity was measured in PPMS using dc resistivity options. Magnetization was measured by means of a vibrating sample magnetometer (VSM) probe equipped with a physical property measurement system (PPMS), Quantum Design, Inc., USA. The temperature dependence of dc conductivity, $\sigma_{dc}(T)$, for ETO and EBTO is shown in the main panel of Fig. 1(c). At room temperature, for ETO the σ_{dc} is $\sim 2 \times 10^{-3}\ \Omega^{-1}\ cm^{-1}$. Interestingly, for EBTO the σ_{dc} increases to $\sim 5 \times 10^{-2}\ \Omega^{-1}\ cm^{-1}$ at room temperature and then decreases dramatically to $\sim 1 \times 10^{-4}\ \Omega^{-1}\ cm^{-1}$ at 77 K. Overall, the $\sigma_{dc}(T)$ for ETO and EBTO signifies IMT with semiconducting-like behavior for the full temperature regime. The inset of Fig. 1(c) compares the magnetization isotherms $M(H)$ at a temperature of 2.5 K for both compounds. The $M(H)$ of ETO increases linearly with magnetic field below 1 T and shows a tendency to saturate above $\mu_0 H = 1.5$ T. For EBTO, the linear field dependence of M is suppressed and the $M(H)$ curve resembles that of a soft ferromagnet. The saturation magnetization (M_S) at 5 T for ETO and EBTO is $6.6 \mu_B$/f.u. and $3.2\ \mu_B$/f.u., respectively. This also suggests that Ba substituted for Eu, and the valence states of Ba and Eu are both 2^+.

III. RESULT AND DISCUSSION

To reveal the mechanism of IMT with Ba substitution, we performed XAS measurements at the SINS beamline (~0.1 eV energy resolution) of the Singapore Synchrotron Light Source at room temperature [24]. Figure 2 shows XAS at Ti $L_{2,3}$ and O K edges for both ETO and EBTO. We start our discussion with XAS at Ti $L_{2,3}$ edges (Ti $2p \rightarrow 3d$) as shown in Fig. 2(a). The main peaks A, B, C, and D are corresponding to Ti L_3-t_{2g}, L_3-e_g, L_2-t_{2g}, and L_2-e_g states, respectively. Because of Ti-O hybridization effects, orbitals (e_g) pointing toward the oxygen ligands yield broader absorption peaks [25]. The overall comparison of Ti XAS shows that the valence state of Ti in both EBTO and ETO is mostly Ti^{4+}. The slight enhancement of spectral weight in between peaks A and B in EBTO reveals that a small fractional of Ti^{3+} appears in EBTO [Ti^{3+} noted with arrows in Fig. 2(a)]. The additional electrons may come from nonstoichiometry of oxygen vacancies. Nevertheless, considering that ETO is highly insulating, the presence of such a small number of Ti^{3+} alone cannot explain the dramatic changes of the room temperature electrical conductivity of EBTO as compared to ETO. Interestingly, a broad satellite peak (label E) is observed on the higher energy of the main peaks [see the inset of Fig. 2(a)]. According to previous studies [26,27], these satellites are influenced by the local symmetry around metal ions (Ti), the crystal-field interaction, and hybridizations between the transition metals d, f, and O p orbitals. Considering that EBTO and ETO have similar local symmetry and crystal-field effects, the enhancement of the satellite peak E in the case of EBTO gives us an important hint that O $2p$-Ti $3d$ hybridization can be evidently boosted with Ba substitution.

The importance of the hybridization phenomenon is strikingly observed in XAS at the O K edge (O $1s \rightarrow 2p$ transition) of ETO and EBTO as shown in Fig. 2(b). Peaks denoted by $A1$

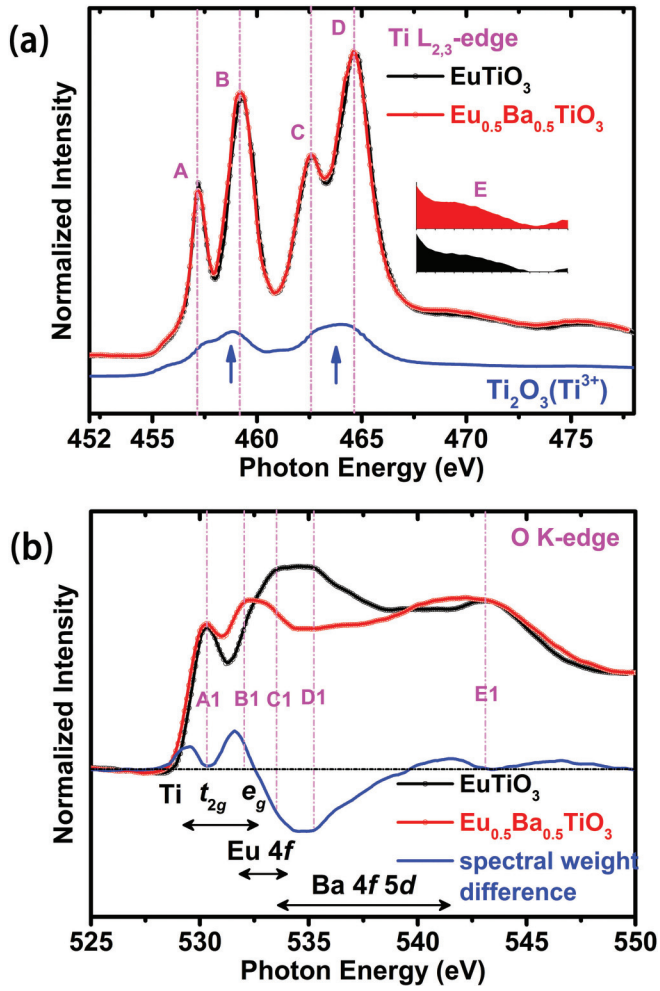

FIG. 2. (a) X-ray absorption at Ti $L_{2,3}$ edges for both $EuTiO_3$ (ETO) and $Eu_{0.5}Ba_{0.5}TiO_3$ (EBTO). The blue line shows Ti^{3+} $L_{2,3}$ XAS taken on a Ti_2O_3 sample, and the arrows mark the maximum intensities of the $L_{2,3}$ edges. The magnification of the inserted satellite (peak E) structures is five times higher than that of the original one. (b) The O K edges XAS for ETO and EBTO. The blue shows the spectral weight difference between ETO and EBTO.

and $B1$ correspond to O $2p$-Ti $3d$ hybridization, whereas peaks $C1$ and $D1$ are attributed to the O $2p$-Eu $4f$ and Ba $4f$,$5d$ hybridizations [12,28]. Note that previous hybrid Hartree-Fock density functional calculations and hard x-ray photoelectron spectroscopy measurements on ETO [28] have shown that the Eu $4f$ states hybridize with the Eu $5d$, Ti $3d$, and O $2p$ states. The energy splitting between $A1$ and $B1$ is ~2.2 eV, which is comparable to that between the t_{2g} and e_g states seen in the Ti L_3 absorption edge, for both samples. Interestingly, significant changes are observed in the whole spectra when comparing EBTO and ETO, demonstrating that the hybridization is dramatically changed by the Ba substitutions. To see the modification in the electronic structures, especially the change in hybridization and unoccupied states, we extract the spectral weight (SW) difference of corresponding spectra collected from EBTO and ETO [see Fig. 2(b)]. For EBTO, the intensities at $C1$ and $D1$ are dramatically reduced, indicating that Ba $4f$-O $2p$ hybridization is much weaker than Eu $4f$-O $2p$ hybridization. In fact, through Ba^{2+} (larger ionic radius than Eu^{2+}) substitution, the bandwidth of the Ti $3d$ and Eu $4f$ states becomes wider and thus the Ti $3d$-O $2p$-Eu $4f$ hybridizations are enhanced. This is also demonstrated by the increased intensities of the $A1$ and $B1$ peaks when substituting Eu by Ba. The anomalous SWT from high-energy bands ($C1$ and $D1$) to low-energy bands ($A1$ and $B1$) is a signature of the electronic screening effects of oxygen [29]. Interestingly, from the SW difference, the XAS shows a new prepeak just below the $A1$ peak, which is consistent with SE results as discussed later. From the observations at the O K edge together with Ti $L_{3,2}$ edge XAS, we reveal that the interplay between orbital hybridizations (Eu-O-Ti) and charge (Ti^{3+}) plays an important role for the increased electrical conductivity in EBTO. The electron introduced by oxygen deficiency is most likely bounded to the Ti-O-Eu hybridized states.

To reveal the electronic correlation effects, we perform SE measurements from ~0.035 to ~6 eV on both ETO and EBTO as a function of temperature. The SE is a powerful technique because it directly measures the complex dielectric function without the need of a Kramers-Kronig transformation [30]. In particular, because this technique fulfills the f-sum rule, one can quantify the SWT [21]. In Fig. 3(a), we show the dielectric functions of ETO and EBTO, along with their difference at room temperature. Five main optical transitions, labeled as A', B', C', and D', and the Drude response are identified. Interestingly, upon Ba substitution, the intensity of A', B', and C' decreases while D' is enhanced accompanied by a new lower energy excitation of Drude response. We noted that this lower-energy excitation leads to a new prepeak just below peak $A1$ shown in XAS [cf. Fig. 2(b)]. Such a broad SWT in SE, which is also consistent with XAS, is a fingerprint of strong electronic correlation [21]. According to previous theoretical calculations [15,16,28], the observed electronic spectral structures can be explained by optical transitions from occupied O $2p$ and Eu $4f$ orbitals to unoccupied Ti $3d$ and Eu $4f^*$ antibonding orbitals. We estimate the optical band gap using the absorption coefficient, which reflects the optical transition performance through extrapolating the linear regimes to $(\alpha h\upsilon)^2 = 0$ [31]. We estimate the optical band gap of ~0.6 and ~0.2 eV for ETO and EBTO, respectively [Fig. 3(c)]. For lower energy spectral weights, they are mainly from the phonon effect and Drude response.

Using a combination of SE and XAS at Ti $L_{3,2}$ and O K edge measurements, we can now identify optical transitions corresponding to A', B', C', and D' for ETO and EBTO at room temperature, and the proposed pictorial model of the electronic band structure is shown in Fig. 3(d). For both ETO and EBTO, the SWTs (A', B', C', and D') are determined by Eu $4f \rightarrow$ Ti t_{2g}/Ti e_g/Eu $4f^*$ transitions, and the intensities of A', B', and C' peaks of EBTO are much weaker than that of ETO due to the decreased ratio of Eu atoms, which then changes the electronic correlation effects in EBTO. Interestingly, the higher energy peak D', which originates from the O $2p \rightarrow$ Ti$3d$ transition, is enhanced. This suggests that the Eu-O-Ti hybridization is reinforced upon Ba substitution. More interestingly, the spectral weight appears in the low-energy region I [inset of Fig. 3(a)] for EBTO, while a

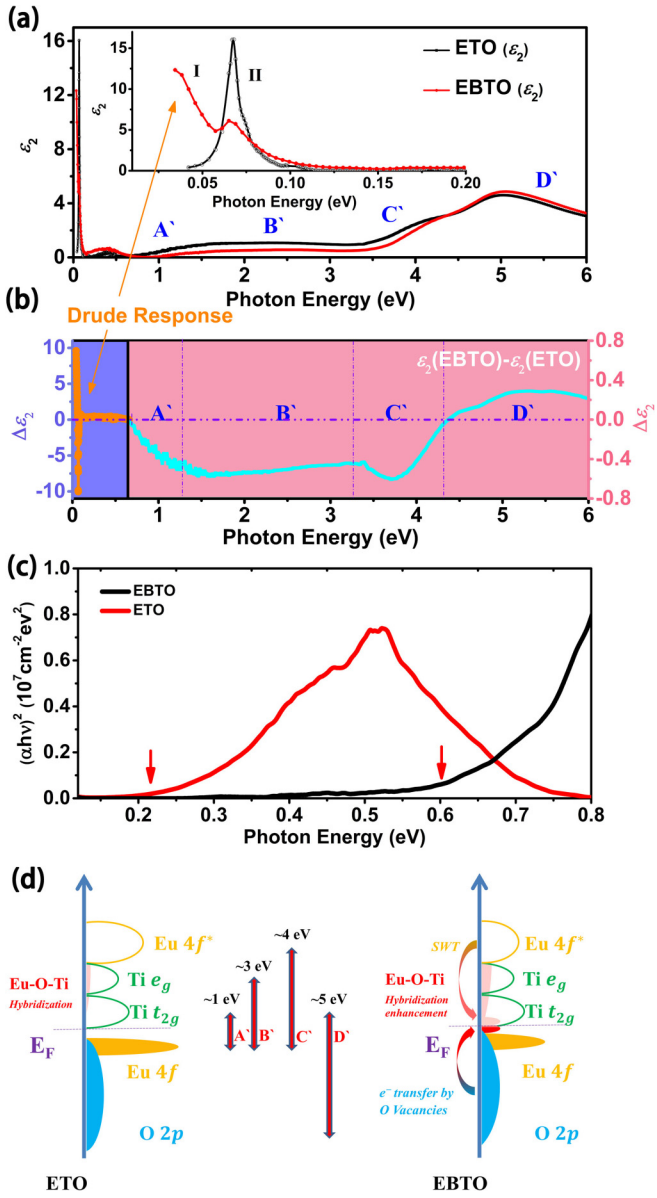

FIG. 3. (a) Dielectric function of ETO and EBTO at room temperature. The inset of (a) shows a zoom-in of the dielectric function below 0.2 eV, and two regions (I and II) are separated for clarity. Region I contains the lowest energy and refers to Drude oscillation. Region II corresponds to the phonon oscillations. (b) The difference of the imaginary part of the dielectric function between ETO and EBTO. (c) The direct band gaps of ETO and EBTO are estimated by extrapolating the linear regimes to $(\alpha h\nu)^2 = 0$. The red arrow indicates the band edge of ETO and EBTO. (d) Schematic representation of the electronic reconstruction process from ETO to EBTO based on the experimental results. The electron transition energies are estimated according to experimental XAS and SE results.

phononlike peak located in region II decreases significantly when compared to ETO. The spectral weight of EBTO in the low-energy region constituted by the Drude response and incoherent charge excitation is completely from the higher-energy region. Due to oxygen vacancies, the SWT occurs from higher- to lower-energy bands and generates a Drude response, which is then responsible for the increased electrical conductivity. The electronic screening effect enhanced Eu-O-Ti hybridization yielded a prominent Drude response and weakened the phonon effect, which makes EBTO become conductive at room temperature [cf. Fig. 3(b)]. Note that based on SE and XAS, the complex dielectric function and the electronic structure of ETO and EBTO are different from $SrTiO_3$ [32–38].

We next study the IMT using temperature-dependent SE, which can reveal the effects of temperature on electronic correlation, particularly the SWT between the high-energy band of O $2p$ and the low-energy band in EBTO. The dielectric function and optical conductivity of EBTO at various temperatures are shown in Figs. 4(a) and 4(b). Interestingly, at low temperature, the SW above 4.5 eV (D' region) increases, while the SW below 4.5 eV (A', B', and C' regions) decreases. This broad SWT in optical conductivity reveals the changes of electronic correlations and hybridizations in EBTO as a function of temperature. To quantitatively characterize the temperature dependence of SWT, we calculate the effective number of electron change (N_{change}) at 77 K as a reference, defined as [39,40]

$$N_{\text{change}}(\Omega_A;\Omega_B) = \frac{2m_0V}{\pi e^2}\int_{\Omega_B}^{\Omega_A}\Delta\sigma_1 d\Omega, \tag{1}$$

where $(\Omega_A;\Omega_B)$, m_0, and V are the cutoff energies, the free-electron mass, and the unit-cell volume, respectively; $\Delta\sigma_1$ is the relative change of optical conductivity with respect to the 77 K data, which are given by

$$\Delta\sigma_1 = \sigma_1(T) - \sigma_1(77\text{ K}), \tag{2}$$

and the results are shown in Fig. 4(c). To identify electron redistributions as a function of temperatures, N_{change} are divided into three regions, namely the low-energy region below 4.5 eV (A', B', and C' regions), the high-energy region above 4.5 eV (D' region), and the full energy region, which are shown in Fig. 4(d). Because the SW in the full energy region is conserved, the low-energy SW below 4.5 eV is then transferred to high-energy SW upon cooling. This low- to high-energy SWT has important implications that it enhances Eu-O hybridization and further increases the screening effect induced by electron-electron interaction, which then suppresses the electrical conductivity.

The low-energy SWT can provide important insight into the origin of IMT as it can reflect the electronic structure and band-gap changes of the samples. Figure 5(a) presents the low-energy dielectric functions at four temperatures of EBTO. Upon cooling, the IMT is accompanied by a SWT from the low-energy to the high-energy region with a significant suppression of low-energy spectral weight yielding an optical band gap at ~0.20 eV [see Fig. 3(c)]. To quantitatively evaluate the temperature dependence of the SWT, we calculate the effective number of electron changes (N_{change}) in comparison with that for 100 K using incremental cutoff energies [(0; 0.06), (0; 0.1), (0; 0.2), (0; 0.4), and (0; 0.6)], and the results can be found in Fig. 5(b). With the increase of the cutoff energy, the temperature dependence of N_{change} becomes small, which suggests that the missing low-energy SW through the IMT transfers to high-energy regions. This is consistent with the SWT occurring in higher energy showing in Fig. 4(d), indicating that the enhancement Eu-O hybridization-induced

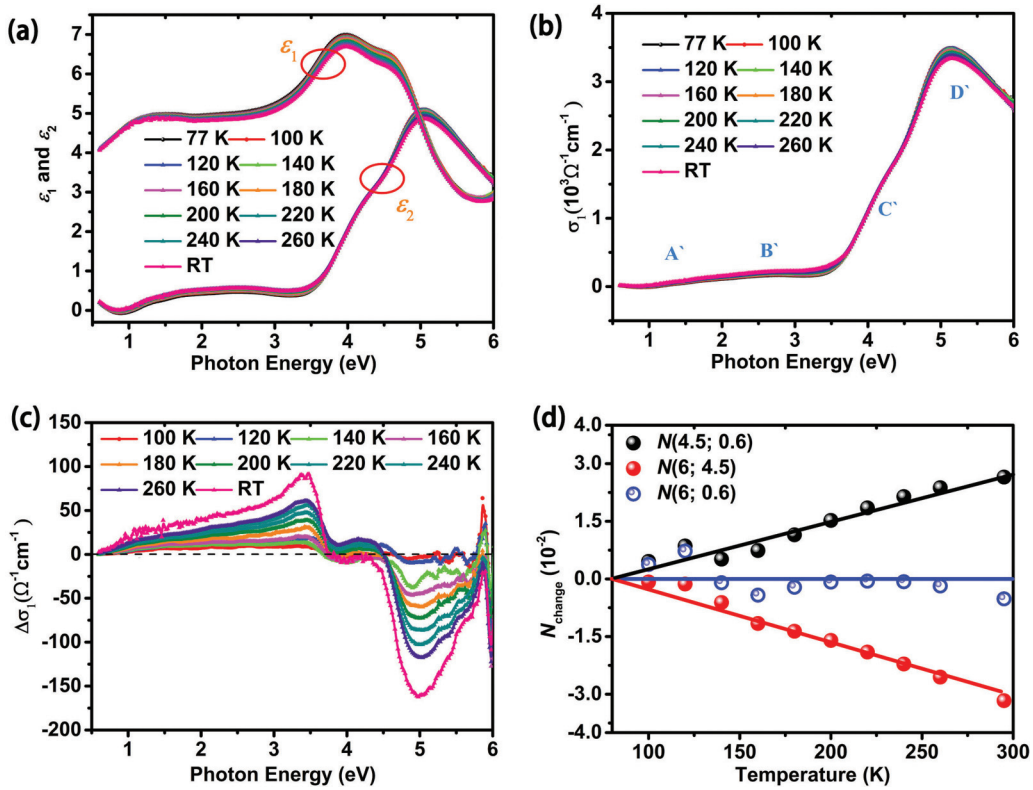

FIG. 4. The temperature-dependent spectroscopic ellipsometry. (a) The real $[\varepsilon_1(\omega)]$ and imaginary $[\varepsilon_2(\omega)]$ dielectric function of EBTO as well as the derived optical conductivity (b) shown by $\sigma(\omega) = i\omega[1 - \varepsilon(\omega)]/4\pi$ with varying temperature. (c) The relative change of optical conductivity with respect to the 77 K data. (d) Effective number of electron change (N_{change}) as a reference of electron number at 77 K. Three regions are calculated: the low-energy region below 4.5 eV (A', B', and C' regions), the high-energy region above 4.5 eV (D' region), and the full energy region.

low- to high-energy SWT is the main underlying mechanism of the IMT for EBTO. Such a SWT over a wide energy range again demonstrates the importance of electronic correlations, especially oxygen electronic screening, and Eu-O-Ti hybridizations in IMT of EBTO. In addition, we also note that the phonon effect is significantly suppressed with increased carrier density at higher temperature [see the inset of Fig. 5(a)]. According to the calculated phonon dispersion of EBTO [5], the phonon that emerged at ~60 meV is mainly caused by relative O-Ti/Eu displacements, and therefore it may be influenced by tunable O-Ti/Eu hybridizations. The reduction of the phonon effect has also been observed in Fig. 3(a) when substituting Eu by Ba, in which the contribution of Eu-O hybridization to the phonon effect is significantly diminished due to the reduced Eu ratio.

IV. CONCLUSION

Based on our SE, XAS, and transport measurements, the electronic structure of EBTO and spectral weight transfers at both low and high temperatures can be drawn as shown in Figs. 5(c) and 5(d). EBTO can be categorized as a charge-transfer gap within the Zaanen-Sawatzky-Allen picture [34]. Interestingly, because the bands near the gap have mostly O $2p$ character (hybridized with Eu $4f$ for the occupied state and with Ti $3d$ for the unoccupied state), this suggests that the system exhibits negative charge-transfer energy [41–44]. It can be seen that upon cooling, a wide-energy-range SWT from low- to high-energy bands occurs due to unscreened electron-electron interaction, which then opens the gap in the oxygen bands and reduces the electrical conductivity. Our result demonstrates that the electronic correlations, especially oxygen electronic screening, and Eu-O-Ti hybridizations play an important role in IMT such as that of EBTO, and the methodology presented here can be used to study IMT in transition-metal oxides in general.

ACKNOWLEDGMENTS

We thank Z. Li, E. Chew, H. Miao, W. Wong, W. Zaw, and C. Lim for technical support. This work is supported by the Singapore National Research Foundation under its Competitive Research Funding (No. NRF-CRP 8-2011-06 and No. R-398-000-087-281), MOE-AcRF Tier-2 (MOE2015-T2-1-099, MOE2015-T2-2-065, MOE2015-T2-2-147, and R-144-000-383-592), NUS YIA, FRC (R-144-000-368-112, R-144-000-346-112, and R-144-000-364-112), and NUS Core Support C-380-003-003-001. The authors would also like to acknowledge the Singapore Synchrotron Light Source (SSLS) for providing the facility necessary for conducting the research. The Laboratory is a National Research Infrastructure under the National Research Foundation Singapore.

X.C. and K.R. contributed equally to this work.

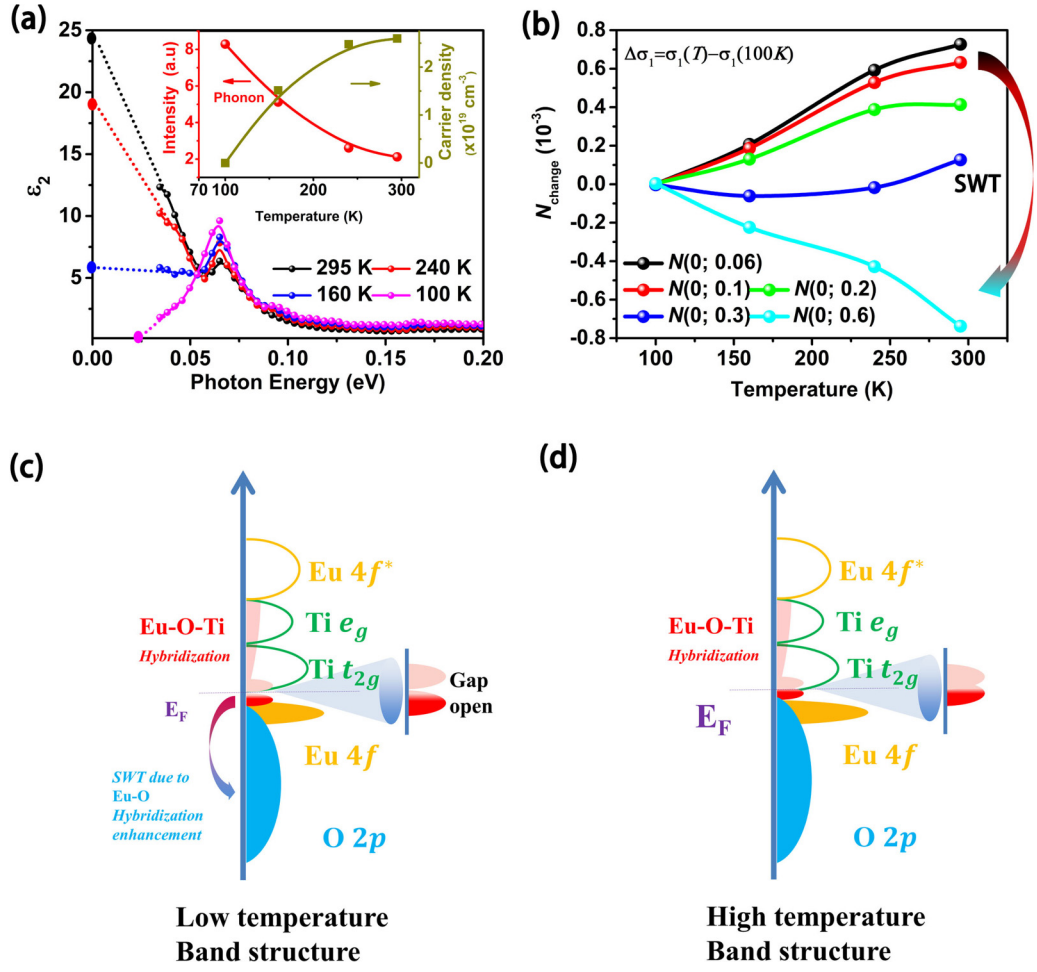

FIG. 5. The temperature-dependent infrared-SE and schematic representation of band structures for EBTO. (a) Temperature dependence of the dielectric functions of EBTO. The inset shows a comparison between the carrier density of region I and the phonon intensity of region II. The dotted lines show the extrapolated photon energy data to zero. (b) Effective number of electron change (N_{change}) as a reference of the electron number at 100 K. Five incremental cutoff energies [(0; 0.06), (0; 0.1), (0; 0.2), (0; 0.4), and (0; 0.6)] are used for calculations. The room temperature N_{change} increases at low energy but reduces at high energy, indicating a low-energy to high-energy SWT through the IMT. Parts (c) and (d) show schematic representations of the electronic reconstruction process from low to high temperature based on the experimental results. The electron transition energies are estimated according to experimental SE results.

[1] M. Izumi, Y. Ogimoto, Y. Okimoto, T. Manako, P. Ahmet, K. Nakajima, T. Chikyow, M. Kawasaki, and Y. Tokura, Phys. Rev. B **64**, 064429 (2001).

[2] Y. Tokura and N. Nagaosa, Science **288**, 462 (2000).

[3] A. Sawa, Mater. Today **11**, 28 (2008).

[4] J. Kuneš, A. V. Lukoyanov, V. I. Anisimov, R. T. Scalettar, and W. E. Pickett, Nat. Mater. **7**, 198 (2008).

[5] C. Kübler, H. Ehrke, R. Huber, R. Lopez, A. Halabica, R. F. Haglund, Jr., and A. Leitenstorfer, Phys. Rev. Lett. **99**, 116401 (2007).

[6] A. Zimmers, L. Aigouy, M. Mortier, A. Sharoni, S. Wang, K. G. West, J. G. Ramirez, and I. K. Schuller, Phys. Rev. Lett. **110**, 056601 (2013).

[7] M. Liu, H. Y. Hwang, H. Tao, A. C. Strikwerda, K. Fan, G. R. Keiser, A. J. Sternbach, K. G. West, S. Kittiwatanakul, and J. Lu, Nature (London) **487**, 345 (2012).

[8] D. McWhan and J. Remeika, Phys. Rev. B **2**, 3734 (1970).

[9] J. B. Torrance, P. Lacorre, A. I. Nazzal, E. J. Ansaldo, and C. Niedermayer, Phys. Rev. B **45**, 8209(R) (1992).

[10] M. Medarde, P. Lacorre, K. Conder, F. Fauth, and A. Furrer, Phys. Rev. Lett. **80**, 2397 (1998).

[11] D. Janes, R. Bodnar, and A. Taylor, J. Appl. Phys. **49**, 1452 (1978).

[12] S. Valencia, A. Crassous, L. Bocher, V. Garcia, X. Moya, R. Cherifi, C. Deranlot, K. Bouzehouane, S. Fusil, and A. Zobelli, Nat. Mater. **10**, 753 (2011).

[13] N. A. Spaldin and R. Ramesh, MRS Bull. **33**, 1047 (2011).

[14] A. O. Sushkov, S. Eckel, and S. K. Lamoreaux, Phys. Rev. A **81**, 022104 (2010).

[15] K. Rushchanskii, S. Kamba, V. Goian, P. Vaněk, M. Savinov, J. Prokleška, D. Nuzhnyy, K. Knížek, F. Laufek, and S. Eckel, Nat. Mater. **9**, 649 (2010).

[16] W. Li, R. Zhao, L. Wang, R. Tang, Y. Zhu, J. H. Lee, H. Cao, T. Cai, H. Guo, and C. Wang, Sci. Rep. **3**, 2618 (2013).

[17] H. Eskes, M. B. J. Meinders, and G. A. Sawatzky, Phys. Rev. Lett. **67**, 1035 (1991).
[18] Y. Ohta, K. Tsutsui, W. Koshibae, T. Shimozato, and S. Maekawa, Phys. Rev. B **46**, 14022 (1992).
[19] M. B. J. Meinders, H. Eskes, and G. A. Sawatzky, Phys. Rev. B **48**, 3916 (1993).
[20] P. Phillips, Rev. Mod. Phys. **82**, 1719 (2010).
[21] A. Rusydi, R. Rauer, G. Neuber, M. Bastjan, I. Mahns, S. Müller, P. Saichu, B. Schulz, S. G. Singer, A. I. Lichtenstein, D. Qi, X. Gao, X. Yu, A. T. S. Wee, G. Stryganyuk, K. Dörr, G. A. Sawatzky, S. L. Cooper, and M. Rübhausen, Phys. Rev. B **78**, 125110 (2008).
[22] X. Yin, M. A. Majidi, X. Chi, P. Ren, L. You, N. Palina, X. Yu, C. Diao, D. Schmidt, B. Wang, P. Yang, M. B. H. Breese, J. Wang, and A. Rusydi, NPG Asia Mater. **7**, e196 (2015).
[23] X. Yin, S. Zeng, T. Das, G. Baskaran, T. C. Asmara, I. Santoso, X. Yu, C. Diao, P. Yang, M. B. H. Breese, T. Venkatesan, H. Lin, Ariando, and A. Rusydi, Phys. Rev. Lett. **116**, 197002 (2016).
[24] A. Rusydi, S. Dhar, A. R. Barman, Ariando, D. C. Qi, M. Motapothula, J. B. Yi, I. Santoso, Y. P. Feng, K. Yang, Y. Dai, N. L. Yakovlev, J. Ding, A. T. S. Wee, G. Neuber, M. B. H. Breese, M. Ruebhausen, H. Hilgenkamp, and T. Venkatesan, Philos. Trans. R. Soc. London, Ser. A **370**, 4927 (2012).
[25] C. Schmitz-Antoniak, D. Schmitz, P. Borisov, F. M. De Groot, S. Stienen, A. Warland, B. Krumme, R. Feyerherm, E. Dudzik, and W. Kleemann, Nat. Commun. **4**, 2051 (2013).
[26] G. van der Laan, Phys. Rev. B **41**, 12366(R) (1990).
[27] M. Mizumaki, A. Agui, K. Yoshii, and M. Nakazawa, Solid State Ion. **172**, 565 (2004).
[28] H. Akamatsu, Y. Kumagai, F. Oba, K. Fujita, H. Murakami, K. Tanaka, and I. Tanaka, Phys. Rev. B **83**, 214421 (2011).
[29] L. H. Yeo, A. Srivastava, M. A. Majidi, R. Sutarto, F. He, S. M. Poh, C. Diao, X. Yu, M. Motapothula, S. Saha, S. Ojha, D. Kanjilal, P. E. Trevisanutto, M. B. H. Breese, T. Venkatesan, and A. Rusydi, Phys. Rev. B **91**, 081112 (2015).
[30] H. Fujiwara, *Spectroscopic Ellipsometry: Principles and Applications* (Wiley, 2007).
[31] D. Schmidt, L. You, X. Chi, J. Wang, and A. Rusydi, Phys. Rev. B **92**, 075310 (2015).
[32] X. Chi, Z. Huang, T. C. Asmara, K. Han, X. Yin, X. Yu, C. Diao, M. Yang, D. Schmidt, P. Yang, P. E. Trevisanutto, T. J. Whitcher, T. Venkatesan, M. B. H. Breese, Ariando, and A. Rusydi, Adv. Mater. **30**, 1707428 (2018).
[33] P. K. Gogoi, L. Sponza, D. Schmidt, T. C. Asmara, C. Diao, J. C. W. Lim, S. M. Poh, S.-i. Kimura, P. E. Trevisanutto, V. Olevano, and A. Rusydi, Phys. Rev. B **92**, 035119 (2015).
[34] P. K. Gogoi, P. E. Trevisanutto, M. Yang, I. Santoso, T. C. Asmara, A. Terentjevs, F. Della Sala, M. B. H. Breese, T. Venkatesan, Y. P. Feng, K. P. Loh, A. H. C. Neto, and A. Rusydi, Phys. Rev. B **91**, 035424 (2015).
[35] K. Han, N. Palina, S. Zeng, Z. Huang, C. Li, W. Zhou, D.-Y. Wan, L. Zhang, X. Chi, and R. Guo, Sci. Rep. **6**, 25455 (2016).
[36] M. Yang, J. Zhou, T. C. Asmara, P. Krüger, X. J. Yu, X. Wang, C. Sanchez-Hanke, Y. P. Feng, T. Venkatesan, and A. Rusydi, ACS Appl. Mater. Inter. **10**, 9774 (2018).
[37] J. Zhou, T. C. Asmara, M. Yang, G. A. Sawatzky, Y. P. Feng, and A. Rusydi, Phys. Rev. B **92**, 125423 (2015).
[38] J. Zhou, M. Yang, Y. P. Feng, and A. Rusydi, Phys. Rev. B **96**, 201406 (2017).
[39] M. K. Stewart, J. Liu, M. Kareev, J. Chakhalian, and D. N. Basov, Phys. Rev. Lett. **107**, 176401 (2011).
[40] T. Asmara, A. Annadi, I. Santoso, P. Gogoi, A. Kotlov, H. Omer, M. Motapothula, M. Breese, M. Rübhausen, and T. Venkatesan, Nat Commun. **5**, 3663 (2014).
[41] J. Zaanen, G. A. Sawatzky, and J. W. Allen, Phys. Rev. Lett. **55**, 418 (1985).
[42] D. D. Sarma, J. Solid State Chem. **88**, 45 (1990).
[43] T. Mizokawa, H. Namatame, A. Fujimori, K. Akeyama, H. Kondoh, H. Kuroda, and N. Kosugi, Phys. Rev. Lett. **67**, 1638 (1991).
[44] D. Khomskii, Lithuanian J. Phys. **37**, 65 (1997).